ACSNANO
Cite This: ACS Nano 2017, 11, 11701-11713
www.acsnano.org
ARTICLE

Donor–Acceptor Conjugated Macrocycles: Synthesis and Host–Guest Coassembly with Fullerene toward Photovoltaic Application

Si-Qi Zhang,[†,‡,¶] Zhen-Yu Liu,[†,¶] Wei-Fei Fu,[§] Feng Liu,[∥] Chuan-Ming Wang,[⊥] Chun-Qi Sheng,[†] Yi-Fei Wang,[†] Ke Deng,[*,‡] Qing-Dao Zeng,[*,‡] Li-Jin Shu,[*,†] Jun-Hua Wan,[*,†] Hong-Zheng Chen,[§] and Thomas P. Russell[#]

[†]Key Laboratory of Organosilicon Chemistry and Material Technology of Ministry of Education, Hangzhou Normal University, Hangzhou 310012, People's Republic of China

[‡]CAS Key Laboratory of Standardization and Measurement for Nanotechnology, CAS Center for Excellence in Nanoscience, National Center for Nanoscience and Technology (NCNST), Beijing 100190, People's Republic of China

[§]State Key Laboratory of Silicon Materials, MOE Key Laboratory of Macromolecular Synthesis and Functionalization, and Department of Polymer Science and Engineering, Zhejiang University, Hangzhou 310027, People's Republic of China

[∥]Department of Physics, Astronomy Shanghai Jiao Tong University, Shanghai 200240, People's Republic of China

[⊥]Shanghai Research Institute of Petrochemical Technology, SINOPEC, Shanghai 201208, People's Republic of China

[#]Polymer Science and Engineering Department, University of Massachusetts, Amherst, Massachusetts 01003, United States

Supporting Information

ABSTRACT: Electron-rich (donor) and electron-deficient (acceptor) units to construct donor–acceptor (D–A) conjugated macrocycles were investigated to elucidate their interactions with electron-deficient fullerene. Triphenylamine and 4,7-bisthienyl-2,1,3-benzothiadiazole were alternately linked through acetylene, as the donor and acceptor units, respectively, for pentagonal 3B2A and hexagonal 4B2A macrocycles. As detected by scanning tunneling microscopy, both D–A macrocycles were found to form an interesting concentration-controlled nanoporous monolayer on highly oriented pyrolytic graphite, which could effectively capture fullerene. Significantly, the fullerene filling was cavity-size-dependent with only one C_{70} or $PC_{71}BM$ molecule accommodated by 3B2A, while two were accommodated by 4B2A. Density functional theory calculations were also utilized to gain insight into the host–guest systems and indicted that the S···π contact is responsible for stabilizing these host–guest systems. Owing to the ellipsoidal shape of C_{70}, C_{70} molecules are standing or lying in molecular cavities depending on the energy optimization. For the 3B2A/$PC_{71}BM$ blended film, $PC_{71}BM$ was intercalated into the cavity formed by the macrocycle 3B2A and provided excellent power conversion efficiency despite the broad band gap (2.1 eV) of 3B2A. This study of D–A macrocycles incorporating fullerene provides insights into the interaction mechanism and electronic structure in the host–guest complexes. More importantly, this is a representative example using D–A macrocycles as a donor to match with the spherical fullerene acceptor for photovoltaic applications, which offer a good approach to achieve molecular scale p–n junctions for substantially enhanced efficiencies of organic solar cells through replacing linear polymer donors by cyclic conjugated oligomers.

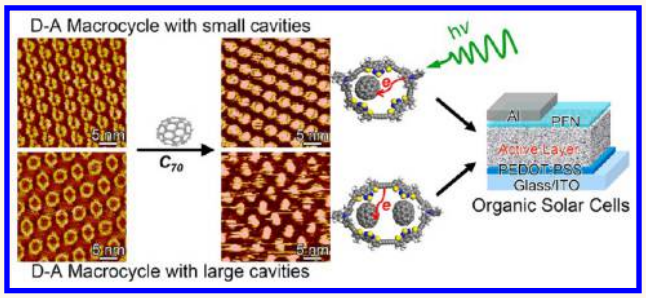

KEYWORDS: *macrocycles, donor–acceptor, host–guest, fullerene, 2D self-assembly, solar cells*

Designing the architecture of donor–acceptor (D–A) pairs is an effective strategy to tailor the electronic structure of polymers for optoelectronic devices, such as organic solar cells (OSCs) and organic field-effect transistors.[1−5] In general, the cyclic structure offers higher symmetry, especially shape-persistent macrocycles, which is potentially more favorable in terms of solid-state packing.[6−10] However, cyclic molecules with uniform structures, such as cycloparaphenylenes (CPPs) and cyclo-[*n*]-thiophenes, offer limited tunability on their electronic structure and prevent their

Received: October 1, 2017
Accepted: November 1, 2017
Published: November 1, 2017

DOI: 10.1021/acsnano.7b06961
ACS Nano 2017, 11, 11701−11713

use in optoelectronic devices.[11−14] Like linear donor−acceptor polymers, introducing D−A motifs to cyclic conjugated backbones can effectively modulate the electronic structure of conjugated macrocycles. To date, only a few D−A conjugated macrocycles have been reported.[15−17] Recently, Nuckolls *et al.* reported that cyclic perylenediimide with a very low LUMO level can serve as a nonfullerene acceptor and outperformed acyclic analogues in OSCs, due to their enhanced crystallinity.[18] It is expected that D−A motifs can be used to tailor the HOMO/LUMO of macrocyclic molecules and will lead to the wide application of cyclic molecules in optoelectronic devices.[19,20]

Another interesting feature of conjugated cyclic molecules is their large molecular cavities, which allow the incorporation of big guest molecules, such as electron-deficient fullerene C_{60} or C_{70}. In the past 10 years, many macrocycles have been developed to study the host−guest interaction with fullerene. Some macrocyclic π-systems, such as CPPs and its derivatives,[21−23] cyclo-[*n*]-thiophene,[24] porphyrin-based macrocycles,[25] and cyclophane ($ExBox_2^{4+}$),[26] have been shown to form strong inclusion complexes with fullerenes. An effective electron transfer between donor receptor and fullerene had been observed in some host−guest systems,[27,28] which have great potential application for organic photovoltaic devices. Recently, covalent organic frameworks (COFs) have emerged as intriguing new materials in OSCs.[29−31] Their porous skeletons provide ideal sites to incorporate fullerene-based acceptors for improved phase separation. However, the nonsoluble nature of this class of material limits their process ability for forming uniform films, which is essential for device fabrication. Additionally, it is not easy to tune the electronic structure of COFs for optoelectronic application. This inspired us to investigate the use of D−A macrocyclic molecules, with engineered orbital levels, as electron donors to absorb sunlight paring with shape-complementary fullerene derivatives as acceptors in typical bulk heterojunction (BHJ) OSCs. As compared to COFs, conjugated macrocycles possess molecular cavities and fully conjugated cyclic backbones. Moreover, cyclic macrocycles could become more soluble by introducing long alkyl chains. Thus, it is desired to fully understand the interaction between D−A conjugated macrocycles and fullerene in their host−guest complexes, as well as their arrangement in the blend. Unfortunately, there is no optoelectronically active conjugated D−A macrocycle being used so far as the donor receptor to incorporate fullerene. This is because the development of D−A macrocycles lagged far behind. The conjugated macrocycles with fullerenes located in the inner cavity undeniably contribute much to donor/acceptor intermixing. The Saturn-like complexes formed by the cyclic conjugated backbone surrounding the spherical fullerene result in much larger intermolecular interfaces.[24]

Considering the electronic properties of D−A conjugated polymers are mainly exploited on substrates, the packing behavior of D−A macrocycles on the two-dimensional (2D) scale is of great importance. The orientation, conformation, packing patterns, and structural defects of the interfacial region between substrate and organic layer have a pronounced effect on their electronic properties, such as carrier mobility. Moreover, the fabrication of regularly ordered host−guest architectures on surfaces may lead to various applications of nanotechnology that depend on the controlled patterning of functional surfaces.[32] Molecular self-assembly, or the so-called "bottom-up" method, has been well recognized as one of the most promising approaches to create functional nanomaterials.[33,34] Scanning tunneling microscopy (STM), a powerful tool in surface science, has an absolute advantage in reflecting the position and distribution of molecules on 2D surfaces or interfaces with their intrinsic submolecular resolution.[35−39] Importantly, for the complicated host−guest systems, the interaction between host molecule and guest molecule can be clearly unraveled.[40−42]

Herein, we introduced an electron-donating triphenylamine (TPA) as a donor unit and an electron-withdrawing 4,7-bis-thienyl-2,1,3-benzothiadiazole ($BTTh_2$) as an acceptor unit into the cyclic backbone. Like other shape-persistent macrocycles, acetylene was used as the linker to produce these cyclic molecules. By modulating the arrangements of D/A units in the cyclic backbone, two macrocycles (**3B2A** and **4B2A**) with different shapes and molecular cavities were synthesized (Scheme 1). Both macrocycles possess a large cavity that is expected to incorporate fullerene. A detailed investigation on the intermolecular interaction between macrocycles and fullerene was performed by fluorescence titration and STM experiments. Theoretical calculation was performed to understand the interaction nature and the electronic structures of these molecules. Additionally, both macrocycles were separately investigated as an electron donor to fabricate BHJ OSCs using $PC_{71}BM$ as the electron acceptor. A combination of X-ray diffraction and scattering techniques was used to characterize the crystalline structure of the macrocycle and the morphology of 3B2A:$PC_{71}BM$ blends.

RESULTS AND DISCUSSION

Synthesis and Characterization. Two different synthetic strategies were used for the synthesis of the two cyclic molecules. By a controllable and stepwise strategy, the **3B2A** macrocycle was synthesized as shown in Scheme 1. The conjugated macrocycle (**3B2A**) with an unsymmetrical structure was obtained at a yield of 21.4% by the palladium−copper-catalyzed homocoupling of alkyne-terminated **M1** under palladium−copper-catalyzed Eglinton−Glaser coupling conditions in dilute solution. Unlike asymmetric **3B2A**, **4B2A**, with a symmetric structure, and was synthesized by means of a fragment-coupling approach. The intermolecular alkyne−alkyne homocoupling reaction between the two C-shaped **M2** fragments produced the **4B2A** macrocycle in an 8.7% yield.

Optoelectronic Properties. In solution, both macrocyclic molecules each showed two distinct absorption bands, a strong band in the shorter wavelength region (320−420 nm) and a weak band in the longer wavelength region (430−600 nm) (Figure 1a and b). Noticeably, a slight red shift (6 nm) of the longer wavelength absorption was observed for **4B2A** relative to **3B2A**. In thin films, both macrocycles exhibited an obvious red shift (25−28 nm) in absorption, suggesting enhanced π−π interaction. However, the absorption spectrum of **4B2A** exhibits almost the same curved profile as that of C-shaped fragment **M2** with no obvious shift (Figure S1), demonstrating that only a weak electronic interaction exists between the units linked by the 1,3-butadiyne bridge. Estimated from the absorption edges, the optical band gaps of the films are 2.1 and 2.0 eV for **3B2A** and **4B2A**, respectively.

As shown in Figure 1, the dilute solutions of both macrocycles exhibited only one fluorescence maximum, with λ_{max} at 612 nm for **3B2A** and 609 nm for **4B2A**. Surprisingly, the fluorescence of both **3B2A** and **4B2A** in film samples showed almost no shift. Both macrocyclic molecules undergo irreversible two-electron oxidations originating from the successive oxidations of the different TPA moieties (Figure S2). The HOMO levels were −5.06 and −5.09 eV for **3B2A** and **4B2A**, respectively. Based on

DOI: 10.1021/acsnano.7b06961
ACS Nano 2017, 11, 11701−11713

Scheme 1. Synthetic Route for 3B2A and 4B2A

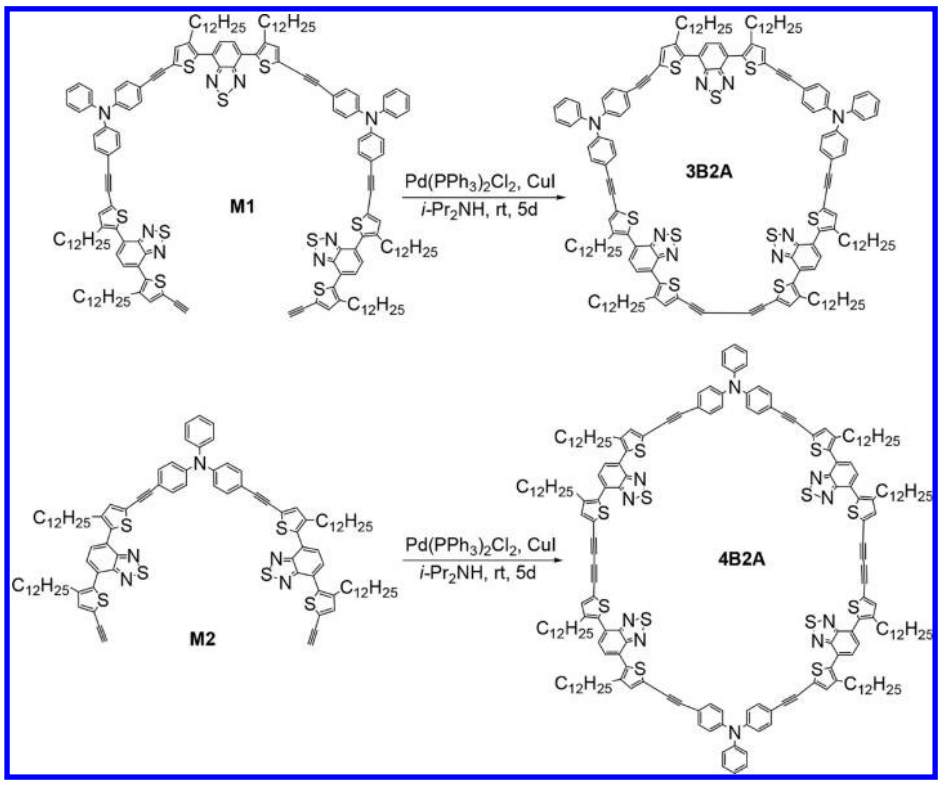

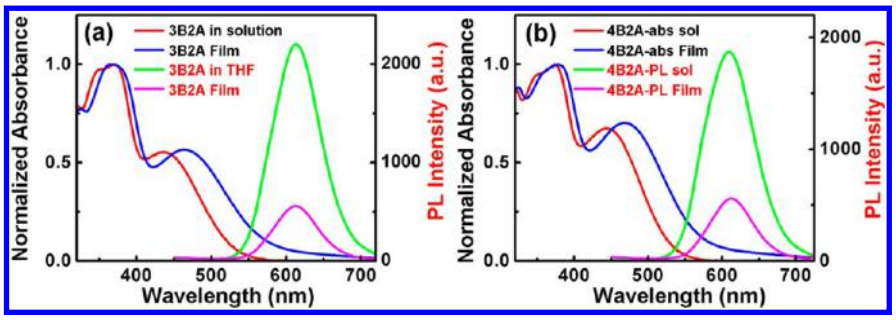

Figure 1. UV/vis absorption spectra in THF solution (red line) and film (blue line) and emission in THF solutions (λ_{ex} = 375 nm, green line) and in solid films (pink line): (a) 3B2A and (b) 4B2A, respectively.

the their optical absorptions in solution, the LUMO levels are determined to be −2.77 eV for **3B2A** and −2.82 eV for **4B2A**. Obviously, only a slight difference in both HOMO/LUMO levels exists between them.

Based on their HOMO/LUMO levels, the two D−A-type cyclic conjugated molecules can be considered typical p-type material. This led us to investigate whether photoinduced electron transfer exists between these macrocycles and highly electron-deficient fullerene (C_{60}, C_{70}) in dilute solution. For both macrocyclic molecules, the fluorescence intensity was quenched with increasing concentration of C_{60} and C_{70} (see Figure 2 and Figure S3 in the SI). The Job plot studies indicated that a 1:2 stoichiometry exists between the macrocycles and C_{60} in toluene (Figure S4). Based on a well-established method, the association constants were calculated as 1.95×10^4 M^{-1} for the **3B2A**−2C_{60} complex and 1.33×10^4 M^{-1} for the **4B2A**−2C_{60} complex. Expectedly, both **3B2A** and **4B2A** showed even stronger binding with C_{70}, which has a much larger size and surface area than C_{60}. As a result, the association constants were enhanced to 2.9×10^4 M^{-1} for the **3B2A**−2C_{70} complexes and 4.3×10^4 M^{-1} for the **4B2A**−2C_{70} complexes. Apparently, the two macrocycles show a strong interaction with fullerene, and a strong photoinduced electron transfer exists between the macrocycle and fullerene. However, these data could not provide a clear picture of how the macrocyclic molecules bind fullerene (C_{60} or C_{70}) in solution. There are two possible situations: one is that the fullerenes are on the outside of the macrocycles and can approach the conjugated skeleton of the macrocycles in or out of the plane of the phenyl rings;[43,44] the other possible situation is that the fullerenes are captured in the inner cavity of the cyclic molecules. The latter case is however much more likely, given that the cavity for both **3B2A** (>1.0 nm) and **4B2A** (>2.0 nm) is large enough to accommodate at least one C_{60} or C_{70}, Therefore, further studies will be needed to identify the structures of these host−guest systems.

Theoretical Insight into Host−Guest Systems of Macrocycles with C_{70} in the Gas Phase. In order to study the possibility of forming host−guest systems with a macrocycle including C_{70}-fullerenes, theoretical calculations in the gas phase performed at the density functional theory (DFT) DMol3 level

DOI: 10.1021/acsnano.7b06961
ACS Nano 2017, 11, 11701−11713

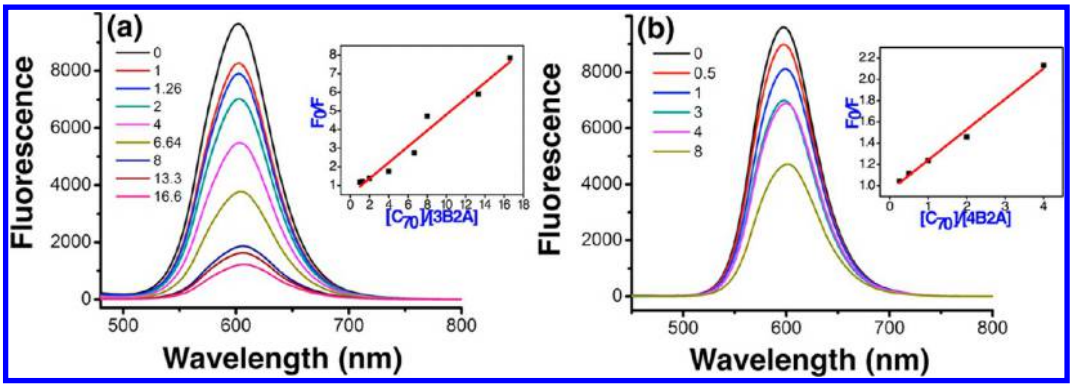

Figure 2. Fluorescence titration of (a) 3B2A and (b) 4B2A with C_{70}, respectively. Inset: Variations of fluorescence intensity F_0/F_{cal} with increasing C_{70} concentration.

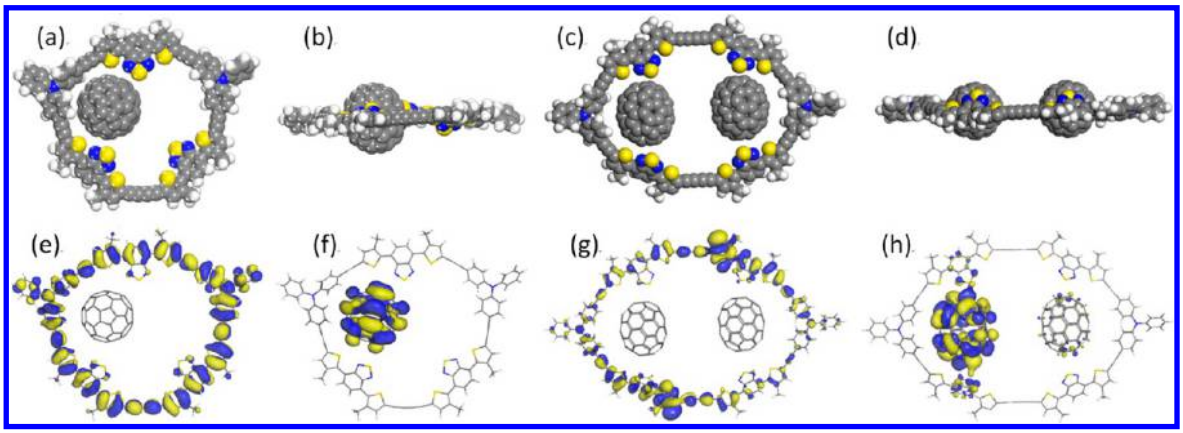

Figure 3. Energy-minimized geometry for 3B2A−C_{70} and 4B2A−2C_{70} complex models. (a) Top view and (b) side view for 3B2A−C_{70}; (c) top view and (b) side view for 4B2A−2C_{70}. Calculated molecular orbitals of complex models derived from the energy-minimized geometry: (e) HOMO, (f) LUMO for 3B2A−C_{70}; (g) HOMO, (h) LUMO for 4B2A−2C_{70}, respectively.

were used to provide a deeper understanding of the origin and nature of the intermolecular forces driving the formation of host−guest systems. Macrocycle−C_{70} and macrocycle−2C_{70} complex models were optimized by using the Perdew−Burke−Ernzerhof (PBE) functional with the dispersion correction (DFT-D). In these models, all long alkyl chains were replaced with methyl groups and only the interactions between guest and host molecule were considered. In the gas phase, the ellipsoidal shape of C_{70} allows multiple distinct geometrical orientations (standing or lying) in these host−guest systems (see Table S1 and Table S2). Specifically, "C_{70}-lying" means that the long axis of C_{70} is parallel to the macrocycle axis, while "C_{70}-standing" implies that the long axis of C_{70} is perpendicular to the macrocycle axis. Stabilization energy is a valid way of measuring the stability and strength of the host−guest interaction. **3B2A** can include only one C_{70} molecule due to the small cavity size (Table S1). Figure 3a and b show the energy-minimized **3B2A**−C_{70} model in which C_{70} is lying. It is clearly seen that C_{70} approaches the sulfur atoms of thiophene and 2,1,3-benzothiadiazole rings in the cyclic backbone and gives rise to a dominant interaction: S···C_{70} contacts. Noticeably, several studies had confirmed that the sulfur atom of the thiophene ring can interact with C_{60} through S···C_{60} (S−π) contacts.[42,45] This is different from the extensively studied [10]-cycloparaphenylene⊃C_{60} host−guest complexes in which concave−convex π−π interactions play a dominant role in the encapsulation.[21] Interestingly, the energy of **4B2A**−2C_{70} is evidently lower than that of **4B2A**−C_{70}, implying that two C_{70} were actually held in the cavity (see Table S2). However, unlike the **3B2A**−C_{70} complex model, in the energy-minimized **4B2A**−2C_{70} model, two C_{70} were standing parallel at the two ends in the cavity of **4B2A** (Figure 3c and d), respectively, and stabilized by S···π interactions. Therefore, the calculation results in the gas phase provided evidence that both macrocycles could encapsulate C_{70} and form very stable host−guest systems, which were mainly stabilized by the S···π interaction.

To get further insight into the electronic structures of **3B2A**−C_{70} and **4B2A**−2C_{70} complexes, the frontier molecular orbitals (MOs) of **3B2A**−C_{70} and **4B2A**−2C_{70} were further calculated and are depicted in Figure 3e,f. For both, the HOMOs were delocalized over the entire cyclic backbone, whereas the LUMOs were localized in fullerene. It is worth noting that the LUMO of **4B2A**−2C_{70} localized in only one of the C_{70} molecules, while LUMO+1 localized in the other. Apparently, the HOMOs of the complexes are associated with the host moieties but independent of the guest moiety, and the LUMOs of the complexes are closely related to the guest moiety but independent of host moieties. This suggests that the lowest energetic electron transition (HOMO → LUMO) would take place from the host to the guest rather than in the interior of the host or guest molecules. As mentioned above, the fluorescence experiments confirmed that the fullerenes can serve as a fluorescence quencher of both macrocycles. Upon irradiation, an electron of the macrocycle is excited onto the fullerene C_{70}, namely, the electron transition of HOMO → LUMO ($S_0 \rightarrow S_1$). Therefore, for the process of emission ($S_1 \rightarrow S_0$), the electron on the fullerene moiety,

DOI: 10.1021/acsnano.7b06961
ACS Nano 2017, 11, 11701−11713

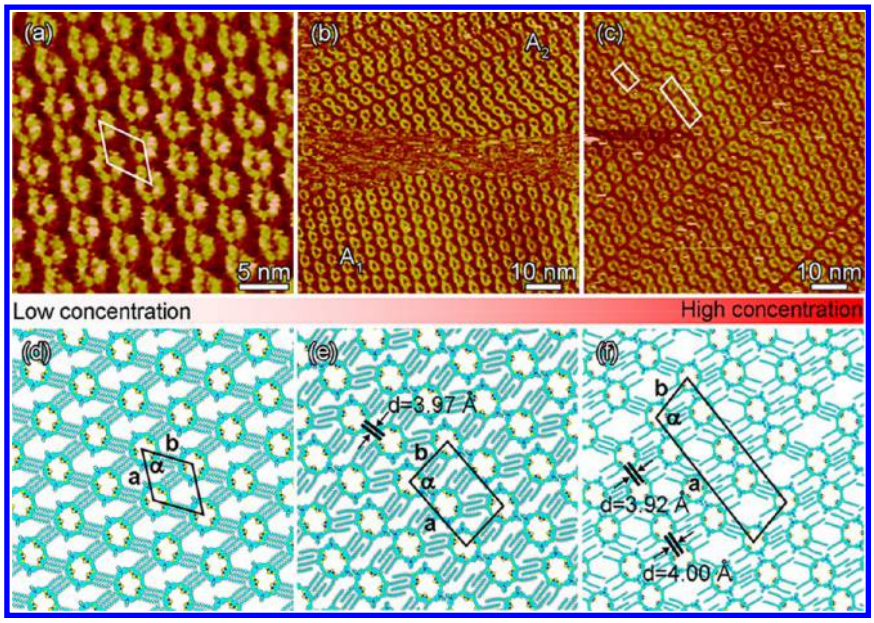

Figure 4. Large-scale STM image of 3B2A molecular self-assembly at the HOPG/1-phenyloctane interface under different solution concentrations and their corresponding calculated models. (a) STM result of 3B2A@c1 solution, I_{set} = 265.5 pA, V_{bias} = 700.1 mV. (b) STM result of 3B2A@c2 solution, I_{set} = 265.5 pA, V_{bias} = 700.1 mV. Two self-assembly patterns were marked by domains A_1 and A_2. (c) STM result of 3B2A@c3 solution, I_{set} = 122.1 pA, V_{bias} = 985.4 mV. (d) Proposed molecular model for 3B2A-low. (e) One of proposed molecular models for 3B2A-high structure (3B2A-high-1). (f) Another proposed molecular model for 3B2A-high structure (3B2A-high-2). The measured units were superimposed on the STM images, and the calculated units were superimposed on the molecular models. Their parameters are all presented in Table 1.

independent of macrocycles, turns back to the HOMO *via* a nonradiation transition, and thus the fluorescence of the macrocycles is quenched. These results imply that the favored photoinduced charge separation exists in these complexes.

Assembly Monolayer and Co-deposition with Guest Molecules. Since macrocycles **3B2A** and **4B2A** including C_{70} are theoretically proved, the coassembly of the macrocycle and C_{70} at the solid/liquid interface should be investigated to verify this guess. First, monolayers of a pure D−A macrocyclic molecule on highly oriented pyrolytic graphite (HOPG) were investigated by STM at the liquid/solid interface. In order to explore how D−A macrocycles interact with fullerene, the co-deposition of cyclic molecules with ellipsoidal C_{70} was further studied. The C_{70} fullerene derivative [6,6]-phenyl-C_{71}-butyric acid methyl ester ($PC_{71}BM$) is the most commonly used electron acceptor in organic solar cells. Therefore, for comparison, $PC_{71}BM$ was also included as a guest molecule in this study.

Concentration-Dependent Monolayer. According to a previous report, concentration variations had a pronounced effect on the arrangements of molecules with long alkyl chains on HOPG. We first carried out concentration experiments for both **3B2A** and **4B2A**. As shown in Figure4b, at **3B2A**@c2 (25% saturation), the **3B2A** molecule appeared as a bright oval circle and exhibited good planarity in the self-assembled nanostructure. The diameter of the inner cavity was from 1.1 to 1.8 nm due to the oval backbone. Interestingly, we could recognize two kinds of self-assembled structures, which were marked by domain A_1 and domain A_2 (Figure 4b). In domain A_1, **3B2A** molecules are present in the form of monomers in an orderly pattern all in the same direction. However, in domain A_2, the **3B2A** molecules tend to take the form of dimers, and the arrangement appeared disordered.

In order to understand the mechanism responsible for the formation of the two different patterns, a lower concentration of **3B2A** solution **3B2A**@c1 (12.5% saturation) and a higher one (**3B2A**@c3) (50% saturation) were used. The corresponding STM results are shown in Figure 4a and c, respectively. The results showed that under lower solution concentration the assembled structure was the same as domain A_1 (denoted by **3B2A**-low) with regular linear structure, while the assembled structure under the higher concentration was similar to domain A_2 (denoted by **3B2A**-high). These results provide compelling evidence that the self-assembly behavior of **3B2A** on the surface was concentration-dependent. The corresponding DFT-calculated model and unit cell for **3B2A**-low is presented in Figure 4d.

As for the **3B2A**-high pattern, albeit with evident disorder in the long range, the distribution of **3B2A** molecules could actually be idealized into two ordered patterns that are mixed with each other. Herein, the **3B2A** dimer as a whole assembled into long arrays. Figure 4c shows that some dimer arrays were closely contacted with each other (denoted by **3B2A**-high-1), while some had a relatively wide ditch with the adjacent arrays (denoted by **3B2A**-high-2). The proposed molecular models for them are superimposed in Figure 4e and f. Parameters of measured unit and calculated unit are all presented in Table 1. The interdistance between two neighboring phenyl groups in the **3B2A** dimer was measured to be 0.39−0.40 nm. It is a $\pi-\pi$ interaction between the phenyl groups of the TPA units from two adjacent macrocyclic molecules that act as the main driving force to dimerize the **3B2A** molecules. However, the van der Waals interaction between interlaced side alkyl chains plays a dominant role in forming the whole self-assembled monolayer.

The **4B2A** molecule appeared as a large olive-shaped circle with an enlarged cavity (diameter from 1.8 to 2.6 nm) and exhibited better symmetry than **3B2A**, as shown in Figure 5a. In Figure 5b, similar to **3B2A**, two kinds of **4B2A** self-assembly structures (domain B_1 and domain B_2) were obviously recognized under **4B2A**@c2 (25% saturation) concentration. After a series of

DOI: 10.1021/acsnano.7b06961
ACS Nano 2017, 11, 11701−11713

Table 1. Experimental (Exptl) and Calculated (Calcd) Lattice Parameters for 3B2A-low, 3B2A-high-1, 3B2A-high-2, 4B2A-low and 4B2A-high

		unit cell parameters		
		a (nm)	b (nm)	α (deg)
3B2A-low	exptl	4.2 ± 0.1	4.2 ± 0.1	60 ± 2
	calcd	4.20	4.20	60.0
3B2A-high-1	exptl	6.5 ± 0.1	4.3 ± 0.1	85 ± 2
	calcd	6.50	4.20	84.5
3B2A-high-2	exptl	14.4 ± 0.1	4.5 ± 0.1	105 ± 2
	calcd	14.40	4.60	103.0
4B2A-low	exptl	10.0 ± 0.1	6.0 ± 0.1	49 ± 2
	calcd	10.05	6.05	49.0
4B2A-high	exptl	4.3 ± 0.1	4.8 ± 0.1	71 ± 2
	calcd	4.20	4.50	73.5

concentration experiments, we could confirm that the loose structure in domain B_1 was denoted as the **4B2A**-low arrangement (Figure 5a), while in the **4B2A**-high arrangement, all molecules closely packed in the same direction, contributing to the structure in domain B_2 (Figure 5c). The unit cells for **4B2A**-low and -high arrangements were also superimposed on the molecular model, respectively, as shown in Figure 5d and e. Analogously, **4B2A** molecules aligned end-to-end with the interdistance between the neighboring phenyl groups of about 0.390 nm. Obviously, the $\pi-\pi$ interaction between the phenyl groups also contributed much to the driving force for the closely packed monolayer of **4B2A**.

Although both macrocycles showed concentration-dependent assembly of structures, we have noticed a little difference between **3B2A** and **4B2A** with respect to their self-assembly behaviors. After performing the experiments several times, we concluded that the **4B2A** self-assembly structures, **4B2A**-low and **4B2A**-high, were both very stable at the corresponding concentration. However, for **3B2A** under low concentration, we observed a structural reconstruction from the **3B2A**-low pattern to the **3B2A**-high pattern with an increase in scanning time. Figure 6a−c show the *in situ* STM study of the time-dependent dynamic process of **3B2A** assembly reconstruction. After adding a droplet of **3B2A**@c1 solution on the freshly cleaved HOPG, the STM tip was immediately immersed into the droplet. The STM images were scanned continuously; each image took 1 min in total. One can clearly see that the **3B2A**-low structure collapsed and then the **3B2A**-high structure formed during STM scanning. Some **3B2A** molecules might have been disturbed by the STM tip during the continuous scanning, indicating that the **3B2A**-low structure was not stable enough to resist external stimulation. This phenomenon did not happen to **4B2A** under the low-concentration condition.

Host−Guest Architectures. A low-concentration **3B2A** solution was first used to construct the host pattern. Upon adding C_{70}, a majority of the hexagonal host−guest pattern, similar to the **3B2A**-low pattern, was obtained. As shown in Figure 7a, C_{70} is the bright spot located in the inner cavity of **3B2A** approaching the boundary of the **3B2A** domain. An uncovered part of every cavity could be observed in the STM image. DFT calculation indicated that only one C_{70} fits into the cavity of the macrocycle and moves toward one side of the inner cavity, which may be stabilized by the interaction between special units on the conjugated backbone and C_{70}. In **3B2A**, the $BTTh_2$ moiety containing both thiophene and 2,1,3-benzothiadiazole units, which can help to stabilize the **3B2A** cavity through S···C_{70} contacts, has been theoretically confirmed. The calculated model is presented in Figure 7c. It was easy to find that the parameters were exactly the same as the **3B2A**-low structure (see Table 2).

Under high **3B2A** concentration conditions, a majority of binary zigzag patterns (Figure 7b) was observed, and the

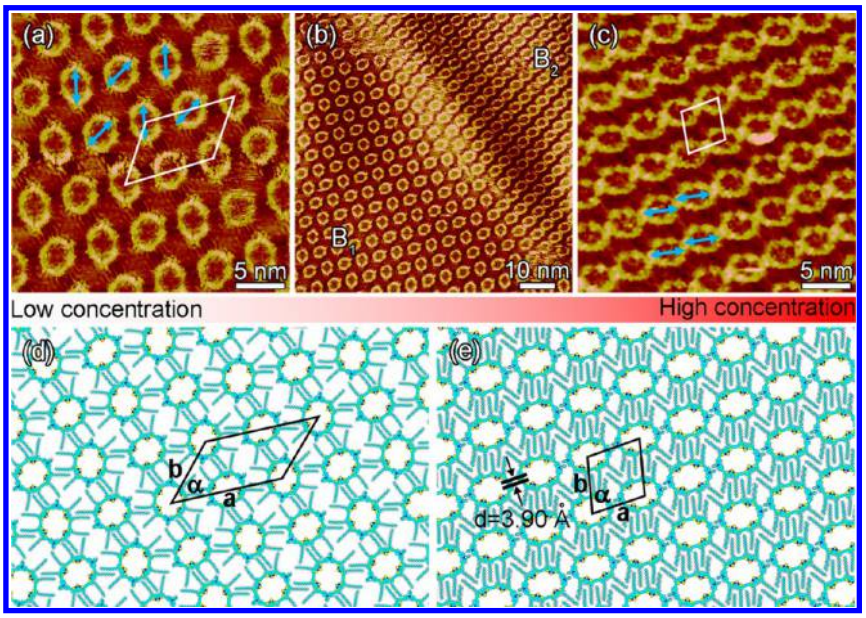

Figure 5. Large-scale STM image of 4B2A molecular self-assembly at the HOPG/1-phenyloctane interface under different solution concentrations and their corresponding calculated models. (a) STM image of 4B2A assembly under 4B2A@c1 (12.5% saturation) concentration, I_{set} = 299.1 pA, V_{bias} = 699.8 mV. The blue arrows show the staggered arrangements of 4B2A molecules with different orientations. (b) STM image of 4B2A self-assembly under 4B2A@c2 concentration, I_{set} = 299.1 pA, V_{bias} = 699.8 mV. Two self-assembled structures are marked by domains B_1 and B_2. (c) STM results of 4B2A self-assembly under 4B2A@c3 (50% saturation) concentration, I_{set} = 188.1 pA, V_{bias} = 826.1 mV. (d) Proposed molecular model for the 4B2A-low structure. (e) Proposed molecular model for the 4B2A-high structure. Parameters of the measured unit and calculated unit are all presented in Table 1.

DOI: 10.1021/acsnano.7b06961
ACS Nano 2017, 11, 11701−11713

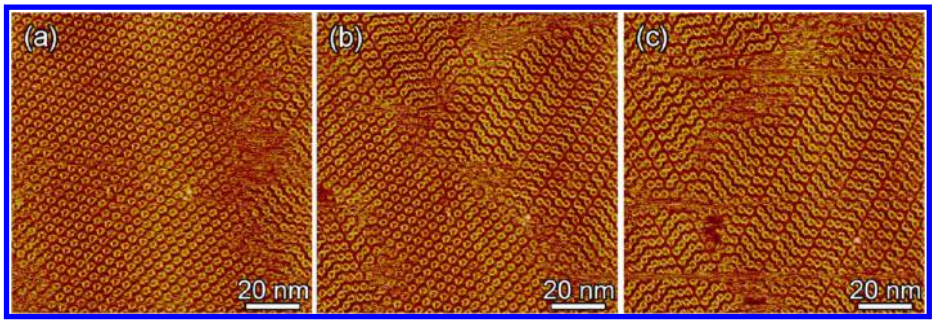

Figure 6. *In situ* STM images of the time-dependent dynamic process of 3B2A assembly reconstruction under low concentrations (3B2A@c1), I_{set} = 299.1pA, V_{bias} = 699.8 mV: (a) t = 1 min, (b) t = 2 min, (c) t = 3 min.

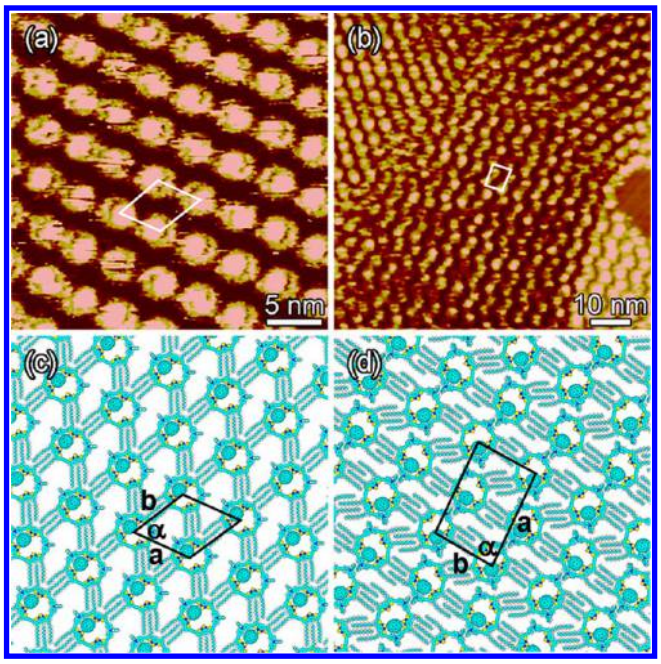

Figure 7. Large-scale STM images and calculated models for the coassembly structure of 3B2A and C_{70} at the HOPG/1-phenyloctane interface. (a) Low-concentration 3B2A coassembly with saturated C_{70}, I_{set} = 122.1 pA, V_{bias} = 941.5 mV. (b) High-concentration 3B2A coassembly with saturated C_{70}, I_{set} = 122.1 pA, V_{bias} = 941.5 mV. (c, d) Corresponding molecular models of 3B2A-low−C_{70} and 3B2A-high−C_{70}, respectively. Parameters of the measured unit and calculated unit are all presented in Table 2.

Table 2. Experimental (Exptl) and Calculated (Calcd) Lattice Parameters for the Host−Guest System on HOPG

		unit cell parameters		
		a (nm)	b (nm)	α (deg)
3B2A-low−C_{70}	exptl	4.1 ± 0.1	4.2 ± 0.1	62 ± 2
	calcd	4.20	4.20	60.0
3B2A-high−C_{70}	exptl	6.4 ± 0.1	4.3 ± 0.1	85 ± 2
	calcd	6.50	4.20	84.5
4B2A-low−C_{70}	exptl	10.1 ± 0.1	6.1 ± 0.1	49 ± 2
	calcd	10.06	6.05	49.0
4B2A-high−C_{70}	exptl	4.2 ± 0.1	4.5 ± 0.1	74 ± 2
	calcd	4.20	4.50	73.5
3B2A−$PC_{71}BM$	exptl	4.2 ± 0.1	4.3 ± 0.1	61 ± 2
	calcd	4.20	4.20	60.0
4B2A−$PC_{71}BM$	exptl	4.3 ± 0.1	4.6 ± 0.1	73 ± 2
	calcd	4.20	4.50	73.5

calculated unit for the proposed molecular model (Figure 7d) is the same as that of the **3B2A**-high-1 structure. Normally, the adsorption from HOPG and intermolecular interaction contribute synergistically to the observed host−guest coassembly. During this process, guest molecules would lead to some adjustment of the host structure to form a more energetically favorable pattern. The **3B2A**-high-2 structure was not energetically favorable with C_{70} in the cavity and preferred to change to a more ordered zigzag **3B2A**-high-1 pattern. We noticed that the hexagonal **3B2A**−C_{70} structure in the upper left domain of Figure 7b had similar unit parameters to the **3B2A**-low−C_{70} structure in Figure 7a. However, as mentioned above, the **3B2A**-low structure was not stable and would turn into a **3B2A**-high structure with an increase in scanning time. This fact suggests that the C_{70} molecule can increase the stabilization of the host **3B2A**-low structure.

Co-assembly of **4B2A** and C_{70} molecules was also carried out. In Figure 8, STM results showed that **4B2A**−C_{70} binary system was separated into different structures under low and high **4B2A** concentration, which are marked by **4B2A**-low−C_{70} (Figure 8a) and **4B2A**-high−C_{70} (Figure 8b). In **4B2A**-low−C_{70}, **4B2A** displayed a similar arrangement to that with **4B2A** alone at low solution concentration. In **4B2A**-high−C_{70}, **4B2A** also appeared as an orderly lamellar arrangement in large scale, and the lattice parameters were the same as the **4B2A**-high structure. Considering the cavity of **4B2A** (1.8−2.6 nm) was big enough to accommodate two C_{70} molecules, it was believed that the larger bar-shaped spots observed in Figure 8a and b consisted of two C_{70} molecules located in the cavity of **4B2A**. In this host−gust system, both C_{70} molecules can be stabilized by S···C_{70} interactions. The DFT-calculated model in Figure 8c and d also confirmed our speculation.

Apparently, both macrocycles can accommodate C_{70} fullerene and, significantly, C_{70} filling is cavity-size-dependent, both of which are in accordance with the theoretical calculation results in the gas phase. The larger **4B2A** formed a 1:2 nanostructure with C_{70}, whereas the **3B2A** macrocycle, with its smaller ring size, formed a 1:1 complex with C_{70} fullerene. This was inconsistent with the result (1:2 complex) from the fluorescence titration study in dilute solution. We inferred that in solution only one C_{70} molecule was located in the inner cavity of **3B2A**. Another C_{70} molecule probably resides outside of the cavity of **3B2A** and approaches the cyclic backbone from a vertical direction in solution, while on the HOPG surface, due to the lack of S···C_{70} (S−π) contacts, this C_{70} molecule outside the macrocycle could not exist stably enough to be detected by STM.

Given that the potential applications of these macrocycles were explored later as photovoltaic donors to pair with $PC_{71}BM$ as acceptor in this article, the co-depositions of macrocycles and

DOI: 10.1021/acsnano.7b06961
ACS Nano 2017, 11, 11701−11713

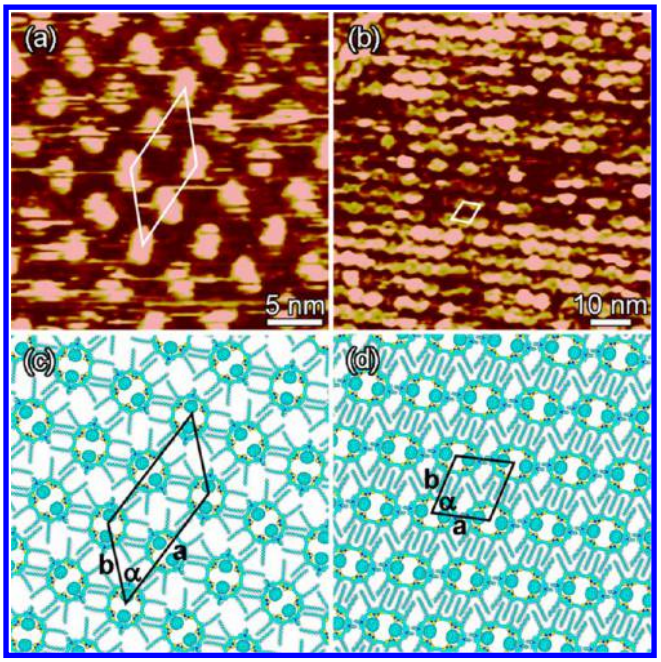

Figure 8. Large-scale STM images and calculated models for the coassembly structure of 4B2A and C_{70} at the HOPG/1-phenyloctane interface. (a) Low-concentration 4B2A coassembly with saturated C_{70}, I_{set} = 147.8 pA, V_{bias} = 831.6 mV. (b) High-concentration 4B2A coassembly with saturated C_{70}, I_{set} = 216.7 pA, V_{bias} = 872.8 mV. (c, d) Corresponding calculated models of 4B2A-low−C_{70} structure and 4B2A-high−C_{70} structure, respectively. Parameters of the measured unit and calculated unit are all presented in Table 2.

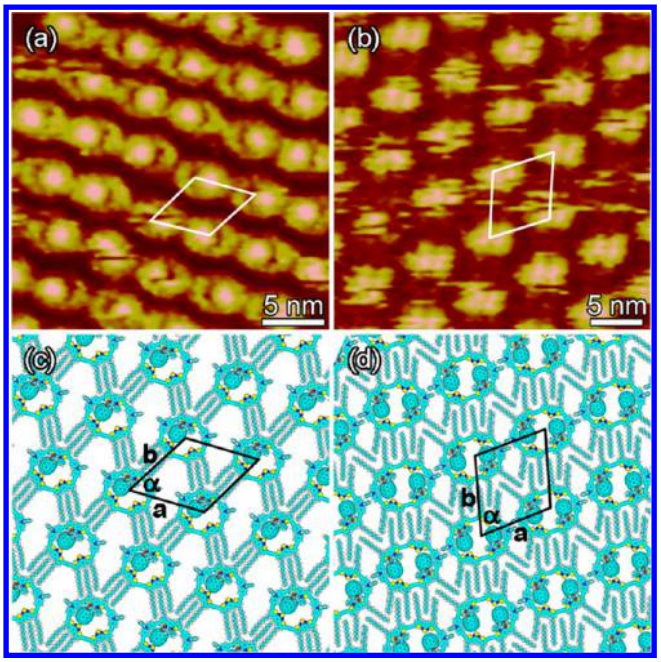

Figure 9. Coadsorption structures of macrocycles with $PC_{71}BM$ guest molecules. (a) STM image of 3B2A−$PC_{71}BM$ pattern. I_{set} = 225.8 pA, V_{bias} = 979.9 mV. (b) STM image of 4B2A−$PC_{71}BM$ pattern. I_{set} = 231.9 pA, V_{bias} = 1026.0 mV. (c, d) Corresponding DFT-calculated models of 3B2A−$PC_{71}BM$ and 4B2A−$PC_{71}BM$, respectively. Parameters of the measured unit and calculated unit are all presented in Table 2.

$PC_{71}BM$ fullerene were also investigated. For both macrocycles, only one binary structure was observed after adding $PC_{71}BM$ (Figure 9a and b). The corresponding model in Figure 9c shows the orderly arrangement of **3B2A** molecules with one $PC_{71}BM$ located in each inner cavity. This arrangement was similar to that of the **3B2A**-low−C_{70} pattern. As shown in Figure 9b, two bright spots were observed in the cavity of each macrocycle, suggesting that the cavity of the **4B2A** molecule was filled with two $PC_{71}BM$ molecules.

Theoretical Investigation on the Formation Mechanism of the Different Assemblies. To better understand and control the self-assembled architecture of pure macrocycles and host−guest systems with C_{70}, simulations were performed by DFT calculations. Different from the calculation in the gas phase (see above), for the calculation of self-assembly on the surface, all long alkyl chains were retained and the interaction between adsorbates and substrate was also considered. The calculated lattice parameters for pure macrocyclic 2D patterns and host−guest systems are summarized in Tables 1 and 2, respectively. The calculated parameters agreed well with the experimental data. In the surface assembly system, the interaction between adsorbates and substrate usually plays an important role. Therefore, we present the total energy (including the interaction energy among adsorbates and the interaction energy between adsorbates and substrate) in Table 3. Generally, a reasonable way to compare the thermodynamic stability of the different arrays should be the total energy per unit area. We also calculated the total energy per unit area of the system (Table 3).

From Table 3, we noticed that the total energy per unit area of **3B2A**-high-1 and **3B2A**-high-2 assembled structures was more thermodynamically stable (−0.119 and −0.102 kcal mol^{-1} $Å^{-2}$) than that of the **3B2A**-low array (−0.088 kcal mol^{-1} $Å^{-2}$). Therefore, we could observe that the percentage of the **3B2A**-high pattern increased at low **3B2A** concentration as a function of scanning time. The calculation results agreed well with our STM observations. On the contrary, we have not observed such transformations from **4B2A**-low to **4B2A**-high, although the total energy per unit area of **4B2A**-low (−0.083 kcal mol^{-1} $Å^{-2}$) is a little higher than that of the **4B2A**-high packing pattern (−0.104 kcal mol^{-1} $Å^{-2}$). By carefully comparing the chemical structures of **3B2A** and **4B2A**, we attributed this difference to their different structural characteristics. Due to its asymmetric pentagonal backbone, **3B2A** had a tendency to correct the imbalance by forming dimers, while for the **4B2A** molecules, in the symmetrical **4B2A**-low pattern, each molecule was fixed by six other molecules, lacking the dynamics factors for this transformation. Considering the flexibility of alkyl chains, the **3B2A** and **4B2A** molecules could be packed loosely or tightly, and thus solution concentration has a great impact on their distribution. It should be noted that the **3B2A**-high-1 and **3B2A**-high-2 patterns, while fairly comparable in the energy of per unit area, can theoretically coexist. Consequently, it was reasonable to regard the **3B2A**-high's disorderly pattern as a combination of two theoretical patterns. For the host−guest systems, besides the interaction among macrocycles, the interaction energy between host macrocycles and guest molecules should also be included, as shown in Table 3. By comparing the total energy per unit area of the host−guest systems with the corresponding pure macrocycle patterns, we noticed that the binary host−guest systems were more thermodynamically stable. The guest fullerene molecules were also adsorbed by HOPG, which contributes to the stabilization of both the **3B2A** and **4B2A** networks.

Photovoltaic Properties. To evaluate the function of the cyclic molecules as electron donor material, BHJ OSCs with a

DOI: 10.1021/acsnano.7b06961
ACS Nano 2017, 11, 11701−11713

Table 3. Total Energy and Energy Per Unit Area for the Pure Macrocycle, Macrocycle−C_{70} Systems, and Macrocycle−$PC_{71}BM$ Systems[a]

	interactions between molecules (kcal mol^{-1})	interactions between molecules and substrate (kcal mol^{-1})	total energy (kcal mol^{-1})	energy per unit area (kcal mol^{-1} Å^{-2})
3B2A-low	−12.216	−121.587	−133.803	−0.088
3B2A-high-1	−26.720	−297.751	−324.471	−0.119
3B2A-high-2	−75.147	−583.039	−658.186	−0.102
4B2A-low	−25.586	−353.460	−379.046	−0.083
4B2A-high	−10.427	−177.256	−187.683	−0.104
3B2A-low−C_{70}	−24.101	−141.645	−165.746	−0.108
3B2A-high−C_{70}	−34.828	−335.387	−370.215	−0.136
4B2A-low−C_{70}	−79.328	−444.089	−523.417	−0.114
4B2A-high−C_{70}	−36.657	−218.710	−255.367	−0.141
3B2A−$PC_{71}BM$	−24.610	−141.154	−165.764	−0.109
4B2A−$PC_{71}BM$	−39.774	−217.756	−257.530	−0.142

[a]The total energy includes the interaction between molecules and the interaction between molecules and HOPG.

Table 4. Summary of the Photovoltaic Performance of Solution-Processed OSCs Based on 3B2A/$PC_{71}BM$ Blends in $CHCl_3$

D/A ratio	annealing temp/°C	V_{oc}/V	J_{sc}/mA·cm^{-2}	FF	PCE/%
1:1	w/o	0.91	2.07	0.25	0.48
1:2	w/o	0.88	3.98	0.29	1.01
1:3	w/o	1.05	4.95	0.33	1.69
1:4	w/o	0.92	6.20	0.32	1.84
1:1	100	1.02	3.22	0.27	0.89
1:2	100	1.02	5.47	0.31	1.72
1:3	**100**	**1.03**	**7.78**	**0.33**	**2.66**
1:4	100	0.96	7.51	0.31	2.21
1:3	120	0.97	6.67	0.31	2.02

device architecture of ITO/PEDOT:PSS/**3B2A**/**4B2A**:$PC_{71}BM$/PFN/Al were fabricated. We found that the D/A ratio was critical for the efficiency of the device. Table 4 shows that different optimized D/A weight ratios were observed for the **3B2A**/$PC_{71}BM$ blends. Notably, power conversion efficiencies (PCEs) increased with a decrease in D/A ratio (from 1:1 to 1:4). The highest PCEs of 1.84% were obtained from a **3B2A**:$PC_{71}BM$ (1:4) for as-cast OSCs. Interestingly, the optimized OSC-based macrocyclic molecule has a much higher $PC_{71}BM$ loading ratio (D/A, 1:4) than most of the reported high-efficient OSCs using high-efficiency linear small-molecular donors (below 1:1).[46,47] Upon thermal annealing, the **3B2A**:$PC_{71}BM$ layer (1:3, w/w) achieved a PCE of 2.66%, which is high considering the absorption of **3B2A** is largely confined to the 300−550 nm range. Moreover, the performance is higher than those based on TPA- and $BTTh_2$-containing linear and star small molecules.[48] We can speculate that $PC_{71}BM$ molecules were intercalated into the cavities of **3B2A** in the blended films, as evidenced by our STM investigation and theoretical calculations. The $J-V$ characteristics and external quantum efficiency (EQE) of optimized devices are shown in Figure S5.

However, a pronounced discrepancy in the final device performance was found between the **3B2A**- and **4B2A**-based OSCs. The highest PCE of 1.28% was obtained from **4B2A**:$PC_{71}BM$ (1:4) upon thermal annealing at 100 °C for 10 min (see Table S3). Probably, structural differences in the host−guest system (only one C_{70} is embedded in the cavity of **3B2A** and two C_{70} are embedded in the cavity of **4B2A**) have substantial effects on the electronic interactions and intermolecular arrangements between the macrocycle donor and fullerene acceptor. However, further study is needed to provide insight into the noticeable differences in device performance for the **3B2A**- and **4B2A**-based OSCs.

It is reasonable to assume that, similar to the intensely studied pBTTT-C_{14}:$PC_{71}BM$ blend consisting of polymer/fullerene bimolecular crystal,[49,50] the macrocyclic molecules were fully intercalated with fullerene in the 1:4 blend with $PC_{71}BM$. This results in the formation of pure $PC_{71}BM$ domains outside the mixed phase, which provides a continuous network to facilitate electron extraction. The pristine film of **3B2A** strongly fluoresced, while $PC_{71}BM$ almost entirely quenched the fluorescence of **3B2A** in blend films (Figure 10). Quenching of

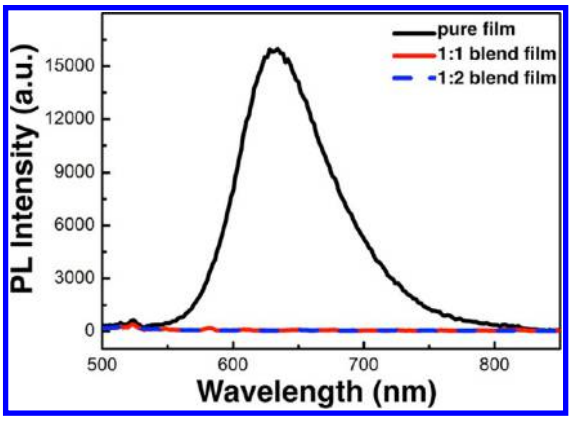

Figure 10. Photoluminescence spectra from the pure film of 3B2A and the 3B2A/$PC_{71}BM$ blended films (1:1, 1:2, wt/wt).

the **3B2A** fluorescence came mainly from the electron transfer from the macrocycle donor to the $PC_{71}BM$ acceptor. Such high quenching efficiencies suggest that excitons travel to the donor/acceptor interface and are separated with high efficiency. Stupp *et al.* had described that hairpin-shaped sexithiophene molecules produced grooved nanowires with PCBM, which could increase the D−A interface, thus enhancing device efficiencies by 23%.[51] In 2013, Dogru *et al.* found that thieno-[3,2-*b*]-thiophene-based porous covalent organic frameworks could accommodate $PC_{61}BM$ and generate a well-ordered electron-donor/acceptor host−guest system for photovoltaic applications despite very low efficiency (PCE < 0.1%).[29]

DOI: 10.1021/acsnano.7b06961
ACS Nano 2017, 11, 11701−11713

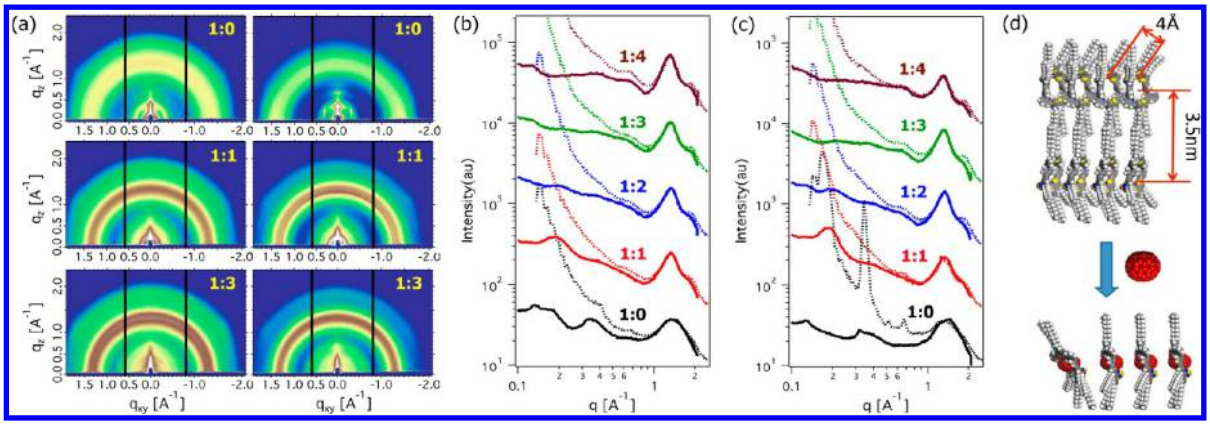

Figure 11. (a) 2D GIXD images of 3B2A and 3B2A:PC$_{71}$BM blend with different processing conditions, left column: as-casted; right column: annealed at 100 °C for 10 min. (b and c) 1D in-plane X-ray profiles extracted from GIXD of as-casted and annealed at 100 °C for 10 min blends, respectively. (d) Suggested molecular models of the assembly structures for 3B2A before and after adding PC$_{71}$BM.

Morphology and Nanostructure. The structure of the **3B2A** macrocycle and its blends with PC$_{71}$BM was investigated by grazing incidence X-ray diffraction (GIXD). The diffraction images and corresponding in-plane (IP) and out-of-plane (OOP) line cut profiles are summarized in Figure 11. As seen from the 2D diffraction image, the as-cast thin film of the smaller ringed **3B2A** showed weak crystalline features. A diffuse diffraction ring was seen at ∼0.35 A^{-1}. There can be some structural features at an even smaller q, in particular at ∼0.16 A^{-1}. Thermal annealing of **3B2A** led to an obvious crystallization. The 0.35 A^{-1} peak showed enhanced intensity in the OOP direction. Higher order peaks could also be observed. From the series of diffraction peaks, the first-order peak should be at 0.18 A^{-1}, which was masked by the beamstop. In the annealed **3B2A** thin film, weak $\pi-\pi$ stacking was found in the IP direction, suggesting a stacking of the phenyl rings parallel to the surface of the film (substrate), *i.e.*, an edge-on orientation. The size of **3B2A** was calculated to be ∼3.5 nm. These data indicate that the **3B2A** ring formed a flat disk, oriented normal to the substrate surface. The 0.18 A^{-1} diffraction in the OOP direction corresponded to the center-to-center distance of 3.4 nm between the rings of **3B2A**, which correlated well with the ring size. When PC$_{71}$BM was added into the **3B2A** thin film (1:1 ratio), the diffraction changed significantly. In the as-cast thin film, a diffraction peak around 0.18 A^{-1} was observed with a weak second-order reflection in the IP direction, which was spread in all directions. Thermal annealing slightly enhanced this diffraction. The addition of PC$_{71}$BM could destroy the ordered organization of **3B2A** especially in the thermally annealed case. We have confirmed that PC$_{71}$BM could favorably interact with **3B2A** and fit into the inner cavity (*vide supra*). Since the PC$_{71}$BM size is much larger than the $\pi-\pi$ stacking distance, the presence of PC$_{71}$BM inside **3B2A** enlarged the disk-to-disk cofacial distance, giving rise to the 1.4 A^{-1} diffraction peak in blends. In the 1:2 (**3B2A**:PC$_{71}$BM) blends, the 0.18 A^{-1} peak still existed, but the intensity became much smaller due, more than likely, to the dilute **3B2A** concentration.

The phase separations of 3B2A:PC$_{71}$BM blends were probed by resonant soft X-ray scattering (RSoXS). As shown in Figure S6, the as-cast BHJ thin films were miscible. Maximum scattering was observed for 1:1 to 1:4 **3B2A**:PC$_{71}$BM blends. This would be expected if PC$_{71}$BM was intercalated into the **3B2A** ring center, suggesting that **3B2A** and PC$_{71}$BM are homogeneously mixed. For the thermally annealed blends, a weak scattering shoulder at ∼0.06 A^{-1}, corresponding to a distance of ∼100 nm, was observed, and increased with higher PC$_{71}$BM loading. This suggests that some embedded PC$_{71}$BM molecules separated from the **3B2A**−PC$_{71}$BM complex to form percolated pathways for electron transport, which could be a major reason for the enhanced device performances.

CONCLUSION

In this study, we alternately installed typical TPA as an electron-rich unit and BTTh$_2$ as an electron-deficient unit into acetylene-linked conjugated macrocycles. STM experiments confirmed that the two shape-persistent cyclic molecules showed interesting concentration-controlled self-assembly behavior at the solid/liquid interface and could capture fullerenes within their inner cavities to form stable complexes in solution. Significantly, the **3B2A** macrocycles, with the smaller ring, formed a 1:1 complex with C$_{70}$ or PC$_{71}$BM fullerene, whereas the larger **4B2A** formed a 1:2 nanostructure with C$_{70}$ or PC$_{71}$BM. The theoretical calculation confirmed that, owing to the ellipsoidal shape of C$_{70}$, different geometrical orientations (standing or lying) are favored in the interface and gas phase. In the **3B2A**/PC$_{71}$BM blended film for OSCs, the PC$_{71}$BM molecules were also intercalated in the inner cavities of the **3B2A** macrocycle and resulted in a power conversion efficiency of 2.66%, which is partially due to the narrow absorption of the macrocyclic donor (300−550 nm). It is believed that further optimizing the electronic structure and extending absorption of this cyclic oligomer by changing the D/A units and linkages will substantially improve the efficiency. The efficient OSCs have been fabricated using D−A conjugated cyclic molecules as donors with fullerene as an acceptor, which results in new donor−acceptor heterojunctions with big shape-complementarity D/A molecular interfaces derived from the host−guest system. More importantly, this work provides further opportunities to achieve high-efficiency OSCs through utilizing D−A conjugated cyclic molecules as donor materials with PCBM to control the morphology of active layer. As shown in the cocrystal of cyclophanes and C$_{60}$,[26] the intercalated fullerenes stack into a 1D array, whereas macrocycles aggregate through $\pi-\pi$ stacking, which can provide favorable percolation pathways for the photogenerated electron and hole.

EXPERIMENT AND COMPUTATIONAL METHODS

General Characterization. NMR spectra were recorded on a Bruker DPX 400 (^{1}H NMR 400, 500 MHz and ^{13}C NMR 100 MHz) spectrometer. The mass spectra were obtained using an Ion-Spec

DOI: 10.1021/acsnano.7b06961
ACS Nano 2017, 11, 11701−11713

4.7 T HiRes MALDI instrument. UV absorption spectra were obtained using a Scinco S-3150 UV/vis spectrophotometer. The photo spectra were measured on an Edinburgh LFS920 fluorescence spectrophotometer. The electrochemical cyclic voltammogram was obtained using a CHI 660C electrochemical workstation with Pt disk, Pt plate, and standard calomel electrode (SCE) as working electrode, counter electrode, and reference electrode, respectively, in a 0.1 mol/L tetrabutylammonium hexafluorophosphate (Bu_4NPF_6) CH_2Cl_2 solution.

STM Measurements. *Sample Preparation.* Shape-persistent macrocycles **3B2A** and **4B2A** were synthesized using the above-mentioned method. Guest molecules C_{70} and $PC_{71}BM$ were purchased from Acros. All the studied samples were dissolved in 1-phenyloctane (Aldrich). All these materials were used without further purification. Highly oriented pyrolytic graphite (grade ZYB) purchased from Agilent (USA) was used as substrate. The samples were prepared by depositing a droplet of the above solution on a basal plane of freshly cleaved HOPG substrate. The samples were studied by STM with the scanning tips immersed directly into the droplet.

STM Measurement. All STM experiments were performed with a NanoscopeIIIa scanning probe microscope system (Bruker, USA) in constant current mode under ambient conditions. STM tips were prepared by mechanically cutting of Pt/Ir wire (80/20). All the STM images provided are raw data and were calibrated by referring to the underlying graphite lattice. Detailed tunneling conditions are given in the corresponding figure captions.

Concentration Experiments. The typical concentrations of the saturated solutions were generally $\sim 10^{-3}$ M. First, a saturated concentration of **3B2A** solution was obtained by dissolving approximately 1.0 mg of **3B2A** solid in 2 mL of 1-phenyloctane. To aid the solubilizing, the solution was put in an ultrasonic bath for 20 min. After sonication, the solution was left unperturbed to equilibrate overnight. The solution was diluted 2-fold subsequent times to prepare concentrations of 12.5%, 25%, and 50% saturation. The same steps were applied to **4B2A**, and the concentrations were at 12.5%, 25%, and 50% saturation. Six pieces of HOPG (grade ZYB, U.S.A.) substrates were freshly cleaved using adhesive tape. A droplet of each solution was deposited on separate HOPG substrates. After the treatments, the samples were studied by STM with its tip immersed directly into the droplet.

Host−Guest Effect Experiments. We used saturated solutions of C_{70} and $PC_{71}BM$ as guest molecules in this experiment. A two-step procedure was carried out: First, after depositing a droplet of **3B2A** solution (25% saturation), the host nanopatterns were formed and observed on the surface of freshly cleaved HOPG; second, a droplet of guest molecule (C_{70} or $PC_{71}BM$) saturated solution was added onto the same HOPG surface. After the treatment, the self-assembled structures of the binary host−guest systems were monitored by STM. The samples of **3B2A** with 50% saturation, **4B2A** (25% saturation), and **4B2A** (50% saturation) were treated similarly.

Device Fabrication and Characterization. Solar cells were fabricated on glass substrates commercially precoated with a layer of indium tin oxide (ITO). Prior to fabrication, the substrates were cleaned using detergent, deionized water, acetone, and isopropyl alcohol consecutively, each for 15 min, and then treated in an ultraviolet ozone generator for 15 min before being spin-coated with a layer of 35 nm PEDOT:PSS. After baking the PEDOT:PSS in air at 140 °C for 15 min, the substrates were transferred to a glovebox. The BHJ layer was spin-cast at 4000 rpm from a solution of donor and acceptor at a total solids concentration of 20 mg mL^{-1}. Subsequently a 5 nm PFN film was deposited on the active layer as a cathode buffer layer. The samples were loaded into a vacuum deposition chamber (background pressure $\approx 5 \times 10^{-4}$ Pa) to deposit a 100 nm thick aluminum cathode with a shadow mask (device area of 5.2 mm^2).

The current−voltage (J−V) curves were measured with Keithley 2400 measurement source units at room temperature in air. The photocurrent was measured under a calibrated solar simulator (Abet 300 W) at 100 mW cm^{-2}, and the light intensity was calibrated with a standard silicon photovoltaic reference cell. The EQE spectrum was measured with a Stanford lock-in amplifier 8300 unit.

Morphology Characterization. Grazing incidence X-ray diffraction characterization of the active layer was performed at beamline 7.3.3, Advanced Light Source (ALS), Lawrence Berkeley National Lab (LBNL). X-ray energy was 10 keV and operated in top off mode. The scattering intensity was recorded on a 2D image plate (Pilatus 2M) with a pixel size of 172 μm (1475 × 1679 pixels). The samples were ∼15 mm long in the direction of the beam path, and the detector was located at a distance of 300 mm from the sample center (distance calibrated by AgB reference). The incidence angle of 0.16° was chosen to optimize the signal-to-background ratio. OPV samples were prepared on PEDOT:PSS-covered Si wafers in a similar manner to the OPV devices, and pure material samples were prepared on Si wafers with a 2 nm natural oxide layer. Resonant soft X-ray scattering experiments were carried out in beamline 11.0.1.2, ALS, LBNL. Experiments were done in transmission geometry. BHJ thin films were floated in water and transferred onto silicon nitride windows from Norcada Inc. Samples were loaded into a high-vacuum chamber ($\sim 10^{-7}$ Torr) to avoid carbon contaminations from the ambient environment. A phonton energy of 285.4 eV was used in running the experiments, which gave the best contrast at the carbon K-edge. Polysterene spheres of 300 nm were used as standard to calibrate sample-to-detector distance.

Calculation Details. *Calculation Method for Self-Assembly on HOPG.* Theoretical calculations were performed using DFT provided by DMol3 code.[52] We used the periodic boundary conditions (PBC) to describe the 2D periodic structure on the graphite in this work. The Perdew and Wang parametrization of the local exchange correlation energy was applied in local spin density approximation (LSDA) to describe exchange and correlation.[53] All-electron spin-unrestricted Kohn−Sham wave functions were expanded in a local atomic orbital basis. For the large system, the numerical basis set was applied. All calculations were all-electron ones and performed with the medium mesh. A self-consistent-field procedure was done with a convergence criterion of 10^{-5} au on the energy and electron density. Combined with the experimental data, we have optimized the unit cell parameters and the geometry of the adsorbates in the unit cell. When the energy and density convergence criterion are reached, we could obtain the optimized parameters and the interaction energy between adsorbates.

To evaluate the interaction between the adsorbates and HOPG, we designed the model system. In our work, the adsorbates are consistent with benzene-ring π-conjugated structures. Since adsorption of benzene on graphite and graphene should be very similar, we have performed our calculations on infinite graphene monolayers using PBC. In the superlattice, graphene layers were separated by 35 Å in the normal direction and represented by orthorhombic unit cells containing two carbon atoms. When modeling the adsorbates on graphene, we used graphene supercells and sampled the Brillouin zone by a 1 × 1 × 1 k-point mesh. The interaction energy E_{inter} of adsorbates with graphite is given by $E_{inter} = E_{tot}$(adsorbates/graphene) − E_{tot}(isolated adsorbates in vacuum) − E_{tot}(graphene).

Calculation in the Gas Phase. All calculations were carried out using the DFT method as implemented in the DMol3 program.[52] Geometries were optimized using the PBE functional with the dispersion correction (DFT-D).[54] The double numerical plus polarization was employed as the basis set, and the real space cutoff distance was 5.0 Å. The core electrons of all atoms were represented by semicore pseudopotentials.[55] The convergence criteria for energy and force were 1×10^{-5} hartree and 2×10^{-3} hartree/Å, respectively.

ASSOCIATED CONTENT

Supporting Information

The Supporting Information is available free of charge on the ACS Publications website at DOI: 10.1021/acsnano.7b06961.

Synthetic route and details of **3B2A** and **4B2A**, ^{1}H and ^{13}C NMR spectra, CV plots of **3B2A** and **4B2A**, fluorescence titration and Job's plot for host−guest complexes, calculated host−guest complex models, J−V and EQE curves, and RSoXS plots for the blend films (PDF)

DOI: 10.1021/acsnano.7b06961
ACS Nano 2017, 11, 11701−11713

AUTHOR INFORMATION

Corresponding Authors

*E-mail: Wan_junhua@hznu.edu.cn.
*E-mail: shulj@hznu.edu.cn.
*E-mail: zengqd@nanoctr.cn.
*E-mail: kdeng@nanoctr.cn.

ORCID

Qing-Dao Zeng: 0000-0003-3394-2232
Jun-Hua Wan: 0000-0003-4061-7403
Thomas P. Russell: 0000-0001-6384-5826

Author Contributions

¶S.-Q. Zhang and Z.-Y. Liu contributed equally.

Notes

The authors declare no competing financial interest.

ACKNOWLEDGMENTS

This work was supported by the National Natural Science Foundation of China (Nos. 21372057, 21472029, 21773041) and the National Basic Research Program of China (No. 2016YFA0200700). T.P.R. was supported by the U.S. Office of Naval Research under contract N00014-15-1-2244. Portions of this research were carried out at beamline 7.3.3 and 11.0.1.2 at the Advanced Light Source, Molecular Foundry, and National Center for Electron Microscopy, Lawrence Berkeley National Laboratory, which was supported by the DOE, Office of Science, and Office of Basic Energy Sciences.

REFERENCES

(1) Dou, L.; Liu, Y.; Hong, Z.; Li, G.; Yang, Y. Low-Bandgap Near-IR Conjugated Polymers/Molecules for Organic Electronics. *Chem. Rev.* **2015**, *115*, 12633−12665.

(2) Müllen, K. Donor-Acceptor Polymers. *J. Am. Chem. Soc.* **2015**, *137*, 9503−9505.

(3) Beaujuge, P. M.; Frechet, J. M. J. Molecular Design and Ordering Effects in π-Functional Materials for Transistor and Solar Cell Applications. *J. Am. Chem. Soc.* **2011**, *133*, 20009−20029.

(4) Wang, C.; Dong, H.; Hu, W.; Liu, Y.; Zhu, D. Semiconducting π-Conjugated Systems in Field-Effect Transistors: A Material Odyssey of Organic Electronics. *Chem. Rev.* **2012**, *112*, 2208−2267.

(5) Zhou, H.; Yang, L.; You, W. Rational Design of High Performance Conjugated Polymers for Organic Solar Cells. *Macromolecules* **2012**, *45*, 607−632.

(6) Moore, J. S. Shape-Persistent Molecular Architectures of Nanoscale Dimension. *Acc. Chem. Res.* **1997**, *30*, 402−413.

(7) Majewski, M. A.; Lis, T.; Cybinska, J.; Stepien, M. Chrysaorenes: Assembling Coronoid Hydrocarbons *via* the Fold-In Synthesis. *Chem. Commun.* **2015**, *51*, 15094−15097.

(8) Luo, J.; Yan, Q.; Zhao, Y.; Li, T.; Zhu, N.; Bai, C.; Cao, Y.; Wang, J.; Pei, J.; Zhao, D. H. A Photoswitch Based on Self-Assembled Single Microwire of a Phenyleneethynylene Macrocycle. *Chem. Commun.* **2010**, *46*, 5725−5727.

(9) Balakrishnan, K.; Datar, A.; Zhang, W.; Yang, X. M.; Naddo, T.; Huang, J. L.; Zuo, J. M.; Yen, M.; Moore, J. S.; Zang, L. Nanofibril Self-Assembly of an Arylene Ethynylene Macrocycle. *J. Am. Chem. Soc.* **2006**, *128*, 6576−6577.

(10) Fischer, M.; Lieser, G.; Rapp, A.; Schnell, I.; Mamdouh, W.; De Feyter, S.; De Schryver, F. C.; Hoger, S. Shape-Persistent Macrocycles with Intraannular Polar Groups: Synthesis, Liquid Crystallinity, and 2D Organization. *J. Am. Chem. Soc.* **2004**, *126*, 214−222.

(11) Iyoda, M.; Shimizu, H. Multifunctional π-Expanded Oligothiophene Macrocycles. *Chem. Soc. Rev.* **2015**, *44*, 6411−6424.

(12) Omachi, H.; Segawa, Y.; Itami, K. Synthesis of Cycloparaphenylenes and Related Carbon Nanorings: A Step toward the Controlled Synthesis of Carbon Nanotubes. *Acc. Chem. Res.* **2012**, *45*, 1378−1389.

(13) Golder, M. R.; Jasti, R. Syntheses of the Smallest Carbon Nanohoops and the Emergence of Unique Physical Phenomena. *Acc. Chem. Res.* **2015**, *48*, 557−566.

(14) Zhang, F.; Götz; Winkler, H. D. F.; Schalley, C. A.; Bauerle, P. Giant Cyclo-[*n*]-thiophenes with Extended π Conjugation. *Angew. Chem., Int. Ed.* **2009**, *48*, 6632−6635.

(15) Kuwabara, T.; Orii, J.; Segawa, Y.; Itami, K. Curved Oligophenylenes as Donors in Shape-Persistent Donor−Acceptor Macrocycles with Solvatofluorochromic Propertie. *Angew. Chem., Int. Ed.* **2015**, *54*, 9646−9649.

(16) Ball, M.; Fowler, B.; Li, P.; Joyce, L. A.; Li, F.; Liu, T.; Paley, D.; Zhong, Y.; Li, H.; Xiao, S.; Ng, F.; Steigerwald, M. L.; Nuckolls, C. Chiral Conjugated Corrals. *J. Am. Chem. Soc.* **2015**, *137*, 9982−9987.

(17) Darzi, E. R.; Hirst, E. S.; Weber, C. D.; Zakharov, L. N.; Lonergan, M. C.; Jasti, R. Synthesis, Properties, and Design Principles of Donor−Acceptor Nanohoops. *ACS Cent. Sci.* **2015**, *1*, 335−342.

(18) Ball, M.; Zhong, Y.; Fowler, B.; Zhang, B.; Li, P.; Etkin, G.; Paley, D. W.; Decatur, J.; Dalsania, A. K.; Li, H.; Xiao, S.; Ng, F.; Steigerwald, M. L.; Nuckolls, C. Macrocyclization in the Design of Organic n-Type Electronic Materials. *J. Am. Chem. Soc.* **2016**, *138*, 12861−12867.

(19) Ball, M.; Nuckolls, C. Stepping into the Light: Conjugated Macrocycles with Donor−Acceptor Motifs. *ACS Cent. Sci.* **2015**, *1*, 416−417.

(20) Zhang, B.; Trinh, M. T.; Fowler, B.; Ball, M.; Xu, Q.; Ng, F.; Steigerwald, M. L.; Zhu, X.-Y.; Nuckolls, C.; Zhong, Y. Rigid, Conjugated Macrocycles for High Performance Organic Photodetectors. *J. Am. Chem. Soc.* **2016**, *138*, 16426−16431.

(21) Iwamoto, T.; Watanabe, Y.; Sadahiro, T.; Haino, T.; Yamago, S. Size-Selective Encapsulation of C60 by [10]-Cycloparaphenylene: Formation of the Shortest Fullerene-Peapod. *Angew. Chem., Int. Ed.* **2011**, *50*, 8342−8344.

(22) Kawase, T.; Tanaka, K.; Fujiwara, N.; Darabi, H. R.; Oda, M. Complexation of a Carbon Nanoring with Fullerenes. *Angew. Chem., Int. Ed.* **2003**, *42*, 1624−1628.

(23) Lee, S.; Chénard, E.; Gray, D. L.; Moore, J. S. Synthesis of Cycloparaphenyleneacetylene *via* Alkyne Metathesis: C70 Complexation and Copper-Free Triple Click Reaction. *J. Am. Chem. Soc.* **2016**, *138*, 13814−13817.

(24) Shimizu, H.; Cojal González, J. D.; Hasegawa, M.; Nishinaga, T.; Haque, T.; Takase, M.; Otani, H.; Rabe, J. P.; Iyoda, M. Synthesis, Structures, and Photophysical Properties of π-Expanded Oligothiophene 8-mers and Their Saturn-Like C60 Complexes. *J. Am. Chem. Soc.* **2015**, *137*, 3877−3885.

(25) Ortiz, M.; Cho, S.; Niklas, J.; Kim, S.; Poluektov, O. G.; Zhang, W.; Rumbles, G.; Park, G. *J. Am. Chem. Soc.* **2017**, *139*, 4286−4289.

(26) Barnes, J. C.; Dale, E. J.; Prokofjevs, A.; Narayanan, A.; Gibbs-Hall, I. C.; Juricek, M.; Stern, C. L.; Sarjeant, A. A.; Botros, Y. Y.; Stupp, S. I.; Stoddart, J. F. Semiconducting Single Crystals Comprising Segregated Arrays of Complexes of C60. *J. Am. Chem. Soc.* **2015**, *137*, 2392−2399.

(27) Calderon, R. M. K.; Valero, J.; Grimm, B.; de Mendoza, J.; Guldi, D. M. Synthesis of Cyclic Porphyrin Trimers through Alkyne Metathesis Cyclooligomerization and Their Host-Guest Binding Study. *J. Am. Chem. Soc.* **2014**, *136*, 11436−11443.

(28) Canevet, D.; Gallego, M.; Isla, H.; de Juan, A.; Perez, E. M.; Martín, N. Enhancing Molecular Recognition in Electron Donor-Acceptor Hybrids *via* Cooperativity. *J. Am. Chem. Soc.* **2011**, *133*, 3184−3190.

(29) Dogru, M.; Handloser, M.; Auras, F.; Kunz, T.; Medina, D.; Hartschuh, A.; Knochel, P.; Bein, T. A Photoconductive Thienothiophene-Based Covalent Organic Framework Showing Charge Transfer Towards Included Fullerene. *Angew. Chem., Int. Ed.* **2013**, *52*, 2920−2924.

(30) Guo, J.; Xu, Y.; Jin, S.; Chen, L.; Kaji, T.; Honsho, Y.; Addicoat, M. A.; Kim, J.; Saeki, A.; Ihee, H.; Seki, S.; Irle, S.; Hiramoto, M.; Gao, J.; Jiang, D. Conjugated Organic Framework with Three-Dimensionally Ordered Stable Structure and Delocalized π Clouds. *Nat. Commun.* **2013**, *4*, 2736.

DOI: 10.1021/acsnano.7b06961
ACS Nano 2017, 11, 11701−11713

(31) Bildirir, H.; Gregoriou, V. G.; Avgeropoulos, A.; Scherfd, U.; Chochos, C. L. Porous Organic Polymers as Emerging New Materials for Organic Photovoltaic Applications: Current Status and Future Challenges. *Mater. Horiz.* **2017**, *4*, 546−556.
(32) Plas, J.; Ivasenko, O.; Martsinovich, N.; Lackinger, M.; Feyter, S. D. Nanopatterning of a Covalent Organic Framework Host-Guest System. *Chem. Commun.* **2016**, *52*, 68−71.
(33) Yoshimoto, S.; Honda, Y.; Ito, O.; Itaya, K. Supramolecular Pattern of Fullerene on 2D Bimolecular "Chessboard" Consisting of Bottom-up Assembly of Porphyrin and Phthalocyanine Molecules. *J. Am. Chem. Soc.* **2008**, *130*, 1085−1092.
(34) Luo, J.; Gao, J.; Wang, A.; Huang, J. Bulk Nanostructured Materials Based on Two-Dimensional Building Blocks: A Roadmap. *ACS Nano* **2015**, *9*, 9432−9436.
(35) Müllen, K.; Rabe, J. P. Nanographenes as Active Components of Single-Molecule Electronics and How a Scanning Tunneling Microscope Puts Them To Work. *Acc. Chem. Res.* **2008**, *41*, 511−520.
(36) De Feyter, S.; De Schryver, F. C. Two-dimensional Supramolecular Self-Assembly Probed by Scanning Tunneling Microscopy. *Chem. Soc. Rev.* **2003**, *32*, 139−150.
(37) May, R.; Jester, S.-S.; Höger, S. A Giant Molecular Spoked Wheel. *J. Am. Chem. Soc.* **2014**, *136*, 16732−16735.
(38) Ruben, M.; Payer, D.; Landa, A.; Comisso, A.; Gattinoni, C.; Lin, N.; Collin, J. P.; Sauvage, J. P.; De Vita, A.; Kern, K. 2D Supramolecular Assemblies of Benzene-1,3,5-Triyl-Tribenzoic Acid: Temperature-Induced Phase Transformations and Hierarchical Organization With Macrocyclic Molecules. *J. Am. Chem. Soc.* **2006**, *128*, 15644−15651.
(39) Ciesielski, A.; Szabelski, P. J.; Rzysko, W.; Cadeddu, A.; Cook, T. R.; Stang, P. J.; Samorì, P. Concentration-Dependent Supramolecular Engineering of Hydrogen-Bonded Nanostructures at Surfaces: Predicting Self Assembly in 2D. *J. Am. Chem. Soc.* **2013**, *135*, 6942−6950.
(40) Zhang, X.; Chen, T.; Yan, H.-J.; Wang, D.; Fan, Q.-H.; Wan, L.-J.; Ghosh, K.; Yang, H.; Stang, P. J. Engineering of Linear Molecular Nanostructures by a Hydrogen-Bond-Mediated Modular and Flexible Host-Guest Assembly. *ACS Nano* **2010**, *4*, 5685−5692.
(41) Zhong, D. Y.; Wedeking, K.; Blömker, T.; Erker, G.; Fuchs, H.; Chi, L. F. Multilevel Supramolecular Architectures Self-Assembled on Metal Surfaces. *ACS Nano* **2010**, *4*, 1997−2002.
(42) MacLeod, J. M.; Ivasenko, O.; Fu, C.; Taerum, T.; Rosei, F.; Perepichka, D. F. Supramolecular Ordering in Oligothiophene-Fullerene Monolayers. *J. Am. Chem. Soc.* **2009**, *131*, 16844−16850.
(43) Mena-Osteritz, E.; Bauerle, P. Complexation of C_{60} on a Cyclothiophene Monolayer Template. *Adv. Mater.* **2006**, *18*, 447−451.
(44) Pan, G.; Cheng, X.; Höger, S.; Freyland, W. 2D Supramolecular Structures of a Shape-Persistent Macrocycle and Co-deposition with Fullerene on HOPG. *J. Am. Chem. Soc.* **2006**, *128*, 4218−4219.
(45) Inoue, R.; Hasegawa, M.; Nishinaga, T.; Yoza, K.; Mazaki, Y. Efficient Synthesis, Structure, and Complexation Studies of Electron-Donating Thiacalix-[*n*]-dithienothiophene. *Angew. Chem., Int. Ed.* **2015**, *54*, 2734−2738.
(46) Zhang, Q.; Kan, B.; Liu, F.; Long, G.; Wan, X.; Chen, X.; Zuo, Y.; Ni, W.; Zhang, H.; Li, M.; Hu, Z.; Huang, F.; Cao, Y.; Liang, Z.; Zhang, M.; Russell, T. P.; Chen, Y. Small-Molecule Solar Cells with Efficiency over 9%. *Nat. Photonics* **2015**, *9*, 35−41.
(47) Van der Poll, T. S.; Love, J. A.; Nguyen, T.-Q.; Bazan, G. C. Non-Basic High-Performance Molecules for Solution-Processed Organic Solar Cells. *Adv. Mater.* **2012**, *24*, 3646−3649.
(48) Li, W. W.; Du, C.; Li, F. H.; Zhou, Y.; Fahlman, M.; Bo, Z. S.; Zhang, F. L. Benzothiadiazole-Based Linear and Star Molecules: Design, Synthesis, and Their Application in Bulk Heterojunction Organic Solar Cells. *Chem. Mater.* **2009**, *21*, 5327−5334.
(49) Miller, N. C. C.; Cho, E.; Junk, M. J. N.; Gysel, R.; Risko, C.; Kim, D.; Sweetnam, S.; Miller, C. E.; Richter, L. J.; Kline, R. J.; Heeney, M.; McCulloch, I.; Amassian, A.; Acevedo-Feliz, D.; Knox, C.; Hansen, M. R.; Dudenko, D.; Chmelka, B. F.; Toney, M. F.; Bredas, J.-L.; McGehee, M. D. Use of X-Ray Diffraction, Molecular Simulations, and Spectroscopy to Determine the Molecular Packing in a Polymer-Fullerene Bimolecular Crystal. *Adv. Mater.* **2012**, *24*, 6071−6079.
(50) Zhang, L.; Liu, F.; Diao, Y.; Marsh, H. S.; Colella, N. S.; Jayaraman, A.; Russell, T. P.; Mannsfeld, S. C. B.; Briseno, A. L. The Good Host: Formation of Discrete One-Dimensional Fullerene "Channels" in Well-Ordered Poly-(2,5-bis-(3-alkylthiophen-2-yl)-thieno-[3,2-b]-thiophene) Oligomers. *J. Am. Chem. Soc.* **2014**, *136*, 18120−18130.
(51) Tevis, I. D.; Tsai, W.-W.; Palmer, L. C.; Aytun, T.; Stupp, S. I. Grooved Nanowires from Self-Assembling Hairpin Molecules for Solar Cells. *ACS Nano* **2012**, *6*, 2032−2040.
(52) Becke, A. D. A Multicenter Numerical-Integration Scheme for Polyatomic Molecules. *J. Chem. Phys.* **1988**, *88*, 2547−2553.
(53) Anastassakis, E. Pressure Tuning of Strains and Piezoelectric Fields In Cubic Superlattices and Heterostructures - Linear Effects. *Phys. Rev. B: Condens. Matter Mater. Phys.* **1992**, *46*, 13244−13253.
(54) Perdew, J. P.; Burke, K.; Ernzerhof, M. Generalized Gradient Approximation made Simple. *Phys. Rev. Lett.* **1996**, *77*, 3865−3868.
(55) Delley, B. Hardness Conserving Semilocal Pseudopotentials. *Phys. Rev. B: Condens. Matter Mater. Phys.* **2002**, *66*, 155125.

DOI: 10.1021/acsnano.7b06961
ACS Nano 2017, 11, 11701−11713